PAPER

A 3D-printed microneedle extraction system integrated with patterned electrodes for minimally invasive transdermal detection†

Changyuan Zhan,‡[a] Fanmao Liu,‡[b] Zhiran Shen,[a] Xinshuo Huang,[a] Shuang Huang,[a] Xiangling Li,[a] Jing Liu,[b] Jiang Yang, [c] Jiefeng Xu,[d] Xi Xie [*a] and Hui-Jiuan Chen [*a]

Point-of-Care-Testing (POCT) is a convenient and timely clinical analysis method, leading the development trend of advanced biosensors. The development of POCT equipment that can achieve minimally invasive percutaneous monitoring can avoid the pain felt by the subjects and achieve *in vivo* and efficient measurement. Here, we reported the development of a microneedle (MN) extraction system based on patterned electrodes, which could provide convenient and minimally invasive detection of bio-analytes (including glucose, pH, and H_2O_2). The 3D-printed hollow MN array was used as a painless transdermal tool, while the interstitial fluid was extracted under negative-pressure conditions. The patterned electrodes could improve the electrochemical performance of the sensor, with the synergistic effect of the micropillar structure to increase the enzyme coating surface area and the nanomaterial electron layer. The patterned electrodes were placed on the back of the MN arrays for electrochemical detection. *In vitro* and *in vivo* studies showed that the MN-extraction system could detect the corresponding bio-analytes in a minimally invasive manner and it did not cause significant tissue damage. The system developed in this work will provide promising technology to expand the application of POCT for minimal tests on interstitial fluids.

Introduction

Point-of-care testing (POCT) enables the analysis of patient specimens near or at the site of patient care, thus enabling clinical decision-making without any delay.[1–3] In recent decades, POCT has been used for self-monitoring of blood glucose levels in patients with diabetes. It has been developed for rapid and efficient monitoring of other diseases, enabling timely treatment by clinicians.[4,5] Advances in microfluidics, lab-on-a-chip methodologies, and medical diagnostic technologies have enabled relentless progress in POCT, providing reliable monitoring of multiple bio-analytes and *in situ*

analysis. POCT has covered the detection range from small molecules with simple structures, such as glucose and lactic acid, to proteins with large molecular weights. Furthermore, POCT-based wearable sensors can provide real-time patient information to enable the tracking of the fluctuation of key health indicators, such as body temperature, pulse rate, blood pressure, and electrocardiogram (ECG) readings, anytime and anywhere. With the rapid progress of wearable technology, wearable sensors have become a powerful component of POCT equipment, enabling non-invasive monitoring of electrophysiological dynamics and disease-related biomarkers. Recently, a variety of wearable sensor devices have emerged with remarkable sensitivity and reliability. For example, a skin-like electronic device has been reported to monitor temperature and timely anti-infection treatment at wound sites with good accuracy.[6] In another study, a mechanically flexible and fully integrated sensor array for multiplexed *in situ* perspiration analysis was also developed. The device provided a real-time assessment of the detailed sweat profile of human subjects who participated in prolonged indoor and outdoor physical activities.[7] In another research work, a printed iontophoretic-integrated fluidic sweat patch was developed that facilitated sweat stimulation, collection, and real-time analysis of sweat ions (sodium, potassium, and pH ions) for on-demand sweat monitoring of human subjects for healthcare appli-

[a]*State Key Laboratory of Optoelectronic Materials and Technologies, Guangdong Province Key Laboratory of Display Material and Technology, School of Electronics and Information Technology, Sun Yat-Sen University, Guangzhou, China. E-mail: chenhuix5@mail.sysu.edu.cn, xiexi27@mail.sysu.edu.cn*

[b]*The First Affiliated Hospital of Sun Yat-Sen University, Guangzhou, China*

[c]*State Key Laboratory of Oncology in South China, Sun Yat-Sen University Cancer Center, Guangzhou, China*

[d]*Key Laboratory of The Diagnosis and Treatment of Severe Trauma and Burn of Zhejiang Province, The Second Affiliated Hospital of Zhejiang University School of Medicine, Hangzhou, China*

†Electronic supplementary information (ESI) available. See DOI: https://doi.org/10.1039/d2bm01975b

‡These authors contributed equally to this work.

cations.[8] However, because the analytes to be tested were discharged from the body through biological secretion, it was difficult to obtain accurate concentration information of the analytes when non-invasive wearable sensors were used to monitor these analytes related to diseases, thus limiting their application in medical care.

Microneedles (MNs) have been widely used in drug delivery[9–13] in the fields of healthcare[10,14–16] and beauty.[17,18] In recent years, their applications have gradually expanded to diagnostic use. The length of MNs is usually within the range of 600–1500 μm, which allows them to penetrate the stratum corneum into the subcutaneous tissue without reaching the nerves and vessels in the deep subcutaneous tissue. This presents a painless and bloodless technology for transdermal applications. MNs are used for the design of diagnostic tools that output bio-analyte-related signals by sensing the sweat,[14,19,20] interstitial fluid (ISF),[21–24] or blood.[25,26] Particularly interesting is ISF, which is a body fluid that provides various health-related biomarkers for biomedical analysis. Like blood, ISF not only contains common metabolites but also contains more specific biomarkers, which are particularly important for the diagnosis of skin diseases (such as melanoma). MN is considered an ideal biosensor platform because it can approach or even extract the subcutaneous fluid in a minimally invasive way to detect various bio-analytes. By adopting a flexible template-based casting method, top-down strategies (such as photolithography) and bottom-up strategies (such as 3D printing, polymer crosslinking), microneedles with different materials (including metals, glass, polymers, and hydrogels) and multiple structures (such as porous microneedles, solid microneedles, and multi-layer microneedles) can be synthesized.[27] Among the above methods, 3D printing is an ideal method due to its advantages of mass production, low cost, and a wide range of materials for choice. Using 3D printing technology, it is possible to fabriacate MNs of various structures with enough high accuracy.

Currently, there are two main methods for MN detection: (1) collecting tissue fluid or blood containing biological analytes using hollow MNs for subsequent testing, and (2) solid MN electrodes for *in situ* detection. Compared to those On-MN electrodes, the extraction–detection technology using hollow microneedles has a wider range of applications, can be compatible with more detection technologies (such as colorimetry,[28] ELISA,[29,30] electrochemistry, and HPLC-MS[31]), and also reduces the difficulty of sensor preparation. Various types of MNs, such as hollow, coated, swelling, and phase transformation, can be designed to break through the stratum corneum and enter the subcutaneous tissue to extract ISF for testing.[32] In one study, the surfaces of solid gold MNs were functionalized with antibodies, and non-structural protein NS$_1$ (an early marker of dengue virus infection) was collected from rats using these antibodies.[33] When inserted into the skin, the functionalized MNs bind to the protein and remain attached. Further *in vitro* analysis is performed after the needles are removed from the animal. Recently, several examples of testing methods involving MNs and electrochemical detection have been reported, including hollow MNs packed with enzyme-filled carbon paste for the amperometric detection of alcohol,[34] and two kinds of metabolites (lactate and glucose, or alcohol and glucose) using multi-channel MN devices.[35] The availability of transdermal diagnostics with MNs has been reported, where solid MN electrodes were modified to enable *in situ* detection. However, the resulting complex processing steps increase the processing difficulty and place restrictions on the integration of sensor arrays. Moreover, MN electrodes suffer from low electrical response due to the small contact area between MNs and the human body. The biocompatibility and stability of the implantable MN electrodes should also be considered for *in vivo* applications.

Given the characteristics of MNs in transdermal access, it will be promising to develop a strategy based on an integrated ISF-extraction sensing system to realize on-demand *in situ* detection. In this study, we developed a MN-extraction system integrated with patterned electrodes that can improve the electrochemical performance of the sensor, with the synergistic effect of carbon nanotubes and conductive polymer materials present on the surfaces of micropillars (Fig. 1). Here, MN arrays were used as painless transdermal tools to readily extract the subcutaneous fluid under negative-pressure conditions, and biosensors placed on the back of the MN arrays generated responding electrical signals for the detection of glucose, H$_2$O$_2$, and pH. The 3D-printed microneedle-extraction system had a simple structure and convenient operation, which was a profit for liquid extraction and measurement. It can also combine advanced detection technologies to expand the detection range from traditional metabolites (such as pH and glucose) to macromolecular biomarkers, such as protein or nucleic acids, which largely expands the application range of microneedle-extraction systems. The patterned electrodes were prepared by photolithography. This method can be used for low-cost mass production and was suitable for commercial practical applications. The micro/nanostructures on the sensor surface significantly improved the detection sensitivity of the electrodes. The MN sensors with applied negative pressure were successfully applied for the detection of multi-bio-analytes in both *in vitro* and *in vivo* measurements. This study provided a unique MN-extraction system with patterned electrodes, which was capable of *in vivo* detection and analysis of bioanalytes in a highly sensitive and minimally invasive manner.

Results and discussion

Characterization of 3D-printed MN arrays

3D printing materials for microneedle applications need to have high processing accuracy in the 3D-printing process, high mechanical strength, and good biocompatibility. Many types of polymer materials can be used for the 3D printing of microneedles.[27,34,36,37] In this study, the 3D-printed microneedle was manufactured with common acrylate-based photopolymer materials for 3D printing. The 3D-printed MN arrays were integrated with three types of sensors as representatives,

Fig. 1 Schematic illustration of the 3D-printed MN-extraction system with patterned electrodes. Schematic description of the system structure and working principle of the MN-extraction system, which could be used as three types of individual biosensors (glucose sensor, pH sensor, and H_2O_2 sensor). The application of vacuum facilitated the extraction of the ISF from the interstitial space. The extracted ISF would be exposed to the integrated patterned biosensor that generated the corresponding electrical signal for the detection of the analytes.

including the glucose MN sensor, pH MN sensor, and H_2O_2 MN sensor. Each type of MN sensors consisted of a single patterned electrode, one MN array and a customized 3D-printed shell. A narrow gas channel on the shell was incorporated for extraction under vacuum pressure while a through hole for placing the biosensor was left on the side of the shell. As shown in Fig. 2A, the MN-extraction system could be integrated with different types of sensors for the detection of different analytes. The MNs used for penetration were arranged in a 2 × 2 needle array, where each microneedle was in a triangular cone shape. To extract the ISF with minimal damage, the length of the microneedle was designed to be 1200 μm. Fig. 2B shows that the MN with each needle tip possessed a cylindrical channel (∅ 100 μm) to enable the liquid to enter. Fig. 2B also shows the sensor sensor integrated with the MN array. The MN arrays were treated with air plasma for better surface wettability (Fig. 2C). Specifically, after treatment, the hydrophilic angle of the material was changed from 73.4° to 37.9°, indicating that hydrophilicity was greatly improved.

Characterization of MN arrays for their penetration into tissue

In order to test the tissue penetration ability of MN arrays, the tips of MN array was coated with rhodamine B to achieve fluorescence labeling (Fig. 2D, left). After 3 min of MN pressing, the penetrating skin developed a distinct fluorescent mark on the surface (Fig. 2D, middle). MN array penetration produced fluorescent patterns and the cross-section fluorescence diagram (Fig. 2D, right) also clearly showed the location of MN tip penetration. The tips of the MN could preserve good morphology after at least three cycles of pression over 20 N against the skin, where no apparent deformation or fracture of the MN tips was observed (Fig. 2E). In the experiment, the MN exhibi-

ted sufficient hardness, which was necessary for skin penetration.

The mechanical test of the MN array penetrating the pig skin was conducted. During the experiment, the MN arrays and pig skin (as skin penetration model) were fixed on the control lever and slide, respectively. The insertion and retraction speed of the control lever was set to 0.29 mm s^{-1}. Fig. 2F illustrates three typical processes of skin penetration: pressing, holding, and retracting. In the process of pressing, the resistance initially showed approximately linear growth and then increased rapidly and nonlinearly. When the resistance reached 2.0 N (the penetration force of each needle was estimated to be 500 mN), obvious penetrating holes were observed on the skin surface, indicating successful penetration. At that time, the loading displacement (3.4 mm) was greater than the length of the MN (1.2 mm), which indicated that when the MN array was applied, the skin would undergo stress deformation. Then, during the 10-second holding process, the resistance gradually decreased to 1.2 N. Finally, in the retracting process, the resistance decreased to 0 N after 3.4 mm load displacement, and the MN lifted upwards to leave the skin. The negative resistance was related to the adhesion between the MN array and the skin. In order to test the extraction performance of MN arrays, their water extraction ability at negative pressure was tested. In six parallel experiments, when negative pressure (15 cmHg) was applied to the MN array sensor, the average amount of water extracted was over 250 mg, which well matched the requirement of the sensing requirements of biosensors (Fig. 2G). As shown in Fig. S7,† the MN coupled with 7.5 cmHg only extracted about 18 mg of water, while the MN without negative pressure barely extracted the water. Therefore, the negative pressure was optimized to be 15 cmHg.
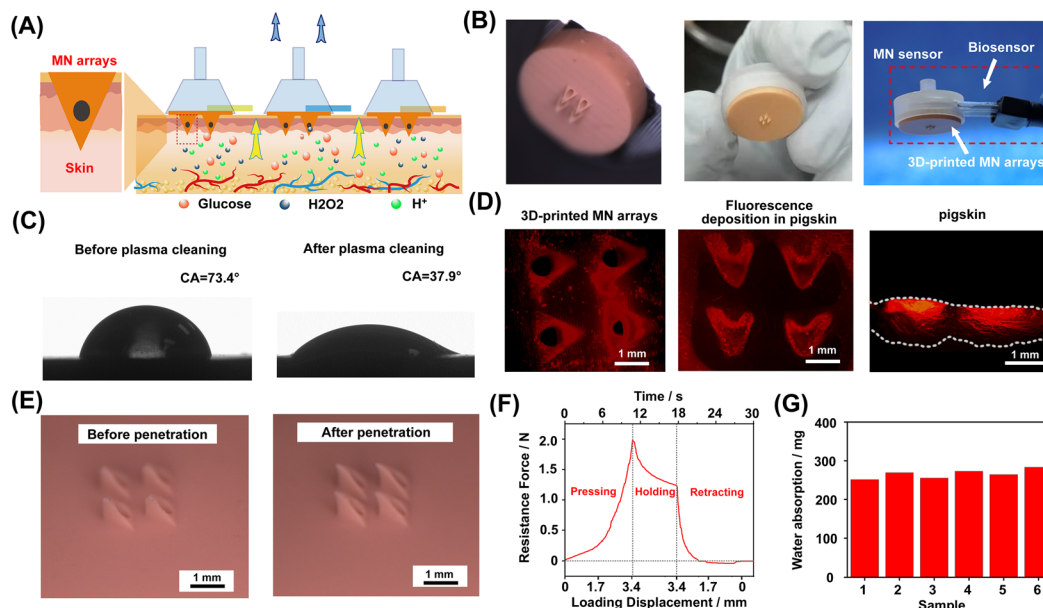
Fig. 2 Characterization and principle of work of 3D-printed MN arrays. (A) MN arrays for extracting the ISF and monitoring glucose, H_2O_2, and pH. (B) MN arrays from different perspectives. (C) Contact angles of water (10 μL) for MN arrays (left) before and (right) after treatment with air plasma. (D) Skin-penetrating properties of MN arrays visualized *via* fluorescence microscopy. Left: pre-stained MN arrays. Middle: penetrated pigskin surface. Right: cross-section of penetrated pigskin. (E) Optical photograph of MN arrays before and after penetration to the skin. (F) Characterization of mechanical properties of MN arrays. (G) Evaluation of water absorption by MN extraction under a negative pressure of 15 cmHg.

Design of electrochemical sensors

Glucose and H_2O_2 sensors were based on typical amperometric sensors, which worked based on a three-electrode system, where Ag/AgCl served as a reference electrode and Pt served as a counter electrode. Glucose in the solution would be oxidized by fixed glucose oxidase (GOx) to produce gluconate lactone and H_2O_2. Then H_2O_2 would decompose under the catalysis of platinum on the electrode surface, which formed a concentration-dependent current that was collected by the electrode. Similarly, the H_2O_2 sensor relied on the current generated by the decomposition of H_2O_2 in the solution. The pH sensor used specific ion-selective electrodes (ISEs), which could adsorb protons reversibly. As the pH of the solution decreased, the absorbed protons would increase and the membrane potential would also increase. According to the Nernst equation, the membrane potential possessed a linear relationship with the pH value of the solution. The pH sensor incorporated two electrodes: a working electrode coated with a conductive proton-selective polymer–polyaniline emeraldine (PANI) and an Ag/AgCl reference electrode. The response voltage of the pH sensor in the physiological pH range conformed to the Nernst equation. In addition, for all biosensor electrodes, sputtering was used to determine the final electrode area (5 mm × 7 mm), followed by modification.

MN sensors integrated with patterned electrodes for transdermal monitoring

The micro-nanostructure was prepared on the surface of the electrodes by photolithography, which improved the surface area for enzyme coating to enhance the detection performance of the sensors (Fig. 3A). During the test, this micro-nanostructure increased the contact reaction between the enzyme and the reaction substrate and enhanced the detection performance of the amperometric sensors. The fabrication process for the patterned substrate is illustrated in Fig. 3B and Fig. S1.† To fabricate the patterned electrode, the cleaned glass slide was first spin-coated with a 20-μm-thick SU-8 photoresist layer. After being soft-baked and exposed to UV using a mask aligner, the glass slide was subjected to a post-exposure bake and developed using an SU-8 developer, followed by post-development baking for half an hour, which generated the SU-8 mold for long-term use. The fabricated SU-8 mold was used for casting with PDMS. An even mixture of PDMS with its curing agent was poured into the SU-8 mold and dried at 80 °C for over 3 h. The as-prepared PDMS film possessed a reverse pattern compared to that of the SU-8 mold. Subsequently, the UV-curable resin liquid was cast into the PDMS film mold and exposed to UV light to prepare the designed pattern. As a result, a well-patterned rigid resin substrate was prepared. The fabricated 20 μm-diameter pillars were well-ordered in an array arrangement, where the space between the cone centers of two pillars was approximately 40 μm. Lastly, the resin substrate was sputtered with Pt to fabricate lead and pad patterns. The resulting cylindrical pattern of electrodes was advantageous for electroactive layer modification due to the increased surface area for enzyme coating.

The glucose sensor relied on an enzyme electrode coated with GOx. To improve electrical performance, the electron transferring mediator layer of MWCNT:PEDOT:PSS was de-
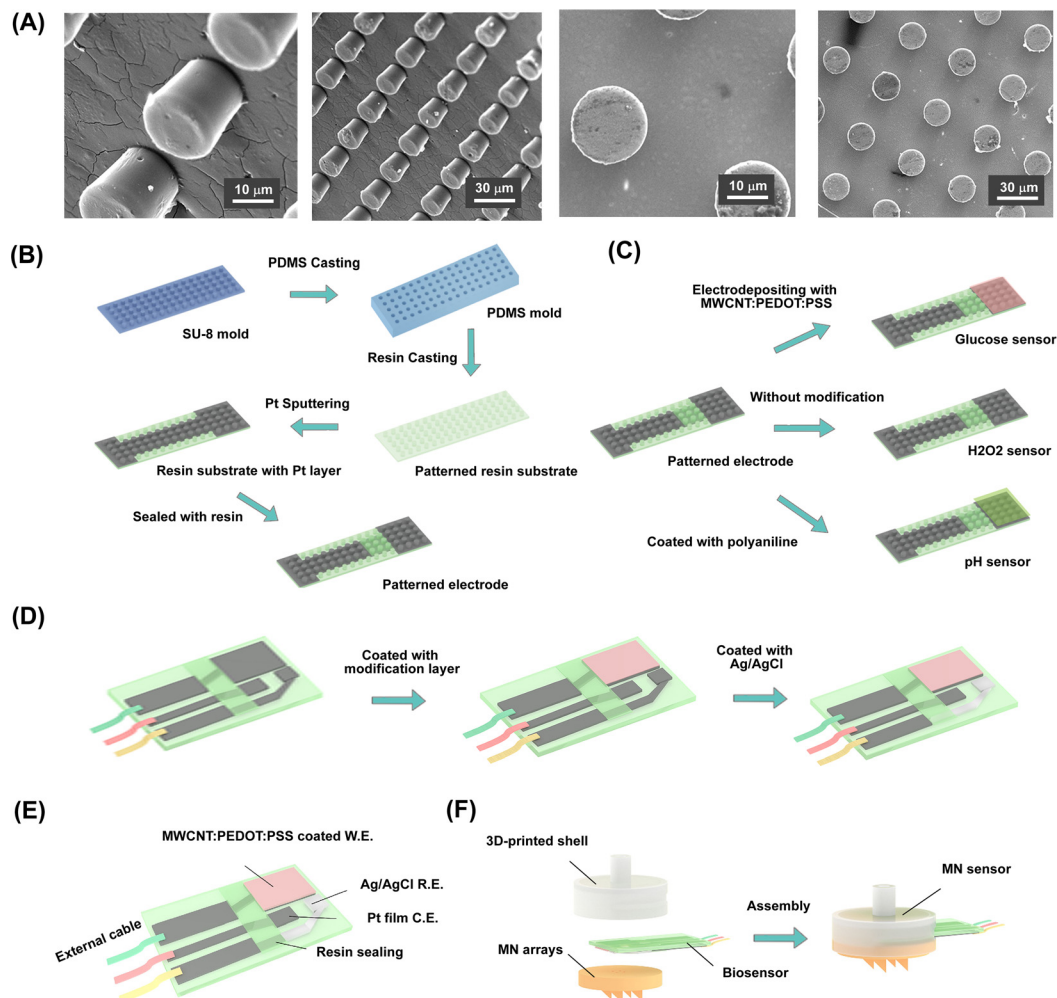
Fig. 3 The preparation process and schematics of the MN sensor. (A) Scanning electron microscopy images of the patterned electrodes at different magnitudes. A cylindrical array with a spacing of 20 μm was shown. (B) Preparation flow chart of patterned electrodes and (C) preparation flow chart of working electrode of biosensors (glucose, H_2O_2, and pH sensors) based on patterned electrodes. (D) Preparation flow chart of an integrated three-electrode-system biosensor. (E) 3D model of the biosensor based on the patterned electrode (using glucose sensor as an example). (F) Assembly diagram of the MN sensor with a patterned electrode.

posited onto the electrode before modification with GOx. The deposited MWCNT:PEDOT:PSS possessed the potential to enhance the electrochemical activity of the electrode. The PEDOT:PSS polymer was a widely used electrochemical electrode modification material due to its excellent conductivity, electrical stability, water solubility, and biocompatibility. In addition, it has been widely reported that multi-walled carbon nanotubes (MWCNTs) have excellent chemical and electrical properties, including excellent conductivity, high electrochemical reaction rates, and large surface areas. Therefore, MWCNTs and PEDOT:PSS as composite membranes could potentially enhance the electrochemical properties of the electrode and improve the affinity of the functional composite membrane coated onto the electrode. When a bias potential was applied, glucose was catalyzed by GOx, producing a detectable current on the electrodes. By contrast, the H_2O_2 sensor relied on Pt to catalyze the decomposition of H_2O_2, an impor-

tant compound of ROS (reactive oxygen species). Therefore, a standard three-electrode system with a Pt working electrode could be used to measure H_2O_2 in the solution. Meanwhile, the pH sensor used PANI as a hydrogen ion-selective membrane to generate a responding potential for quantifying the pH.

The preparation of the biosensors was based on the patterned resin substrates, as shown in Fig. 3C. Different modifications were applied to the electrodes depending on the target analytes. Furthermore, Pt sputtering and Ag/AgCl modification on the same electrode substrate was performed to create the working, counter, and reference electrodes, respectively (Fig. 3D). The patterned electrode attached to the back of the MN array could access the ISF extracted through the hollow channels in the MN tips. To achieve reliable electrochemical measurements, it was necessary to verify the electrochemical performance of the biosensors first before MN integration.

The fabricated biosensors based on patterned electrodes were evaluated in PBS (pH 7.2) and subsequently validated on the *in vitro* skin model.

Electrical characterization of patterned electrode sensors

The analytical response of the glucose biosensor was evaluated based on the current response signal in PBS with different concentrations of glucose. Firstly, the cyclic voltammetry scanning of the glucose biosensor in 10 mM glucose was carried out. Cyclic voltammetry scanning in glucose/$K_3[Fe(CN)_6]$ solution was performed in the potential range from −0.2 to 0.8 V. The glucose sensor modified with the MWCNT:PEDOT:CNT film generated an obvious amperometric response in cyclic voltammetry scanning than the two unmodified glucose sensors (Fig. 4A). Fig. S2A† illustrates the cyclic voltammetry in the $K_3[Fe(CN)_6]$ solution with an increasing glucose concentration, which was measured using the glucose sensor. In cyclic voltammetry, stronger oxidation peaks were observed at 0.4 V potential with increased glucose concentration from 1 mM to 20 mM. Fig. 4B illustrates the amperometric responses measured using the glucose sensor coated with MWCNT:PEDOT:CNT and the polyurethane (PU) layer. The PU layer modified by the drop-casting process provided a wider range of linear responses to glucose. As shown in Fig. 4C, the patterned electrode sensors exhibited a higher sensitivity to glucose than the unpatterned glucose sensor because of the large sensing area and the enhanced electron transmission process. Moreover, the patterned electrode sensor coated with

MWCNT:PEDOT:CNT demonstrated increased sensitivity to glucose compared with the unmodified patterned glucose. The electrode with PU film coating provided a linear response from 1 to 20 mM (the sensitivity was 1.92 μA mM^{-1} with a correlation coefficient of $R^2 = 0.996$). The selectivity of the glucose sensor was evaluated based on the chronoamperometric response in the presence of common interferents in PBS. Fig. 4D visualized the current response of the glucose sensor to 10 mM glucose in the presence of 10 mM lactate, KCl and urea. The influence of each interference factor in the selectivity study of the three types of sensors was quantified, as shown in Fig. S5A–C.† The effect of these coexisting compounds on the response signal of the glucose sensor was less than 5%.

For the H_2O_2 sensor, the detection of H_2O_2 detection was evaluated in PBS with different concentrations of H_2O_2. First, in PBS solution with different concentrations of H_2O_2, cyclic voltammetry scanning was performed at 100 mV s^{-1} in the potential range of −1.0 to 0.1 V. An obvious reduction peak was observed in the cyclic voltammetry results from −0.3 to −0.6 V. With the increase of concentration, the reduction peak moved to a lower potential (Fig. 4E). Therefore, the sensing of H_2O_2 was carried out at a bias potential of −0.45 V. As shown in Fig. 4F, when −0.45 V negative potential was applied, the patterned electrode sensor presented a linear response to H_2O_2 in the range of 0–20 mM. The sensitivity of the H_2O_2 sensor based on the corresponding calibration plot was 35 μA mM^{-1} ($R_2 = 0.997$, relative standard deviation RSD = 0.18%, $n = 5$), as shown in Fig. S3A and B.† In addition, the reproducibil-
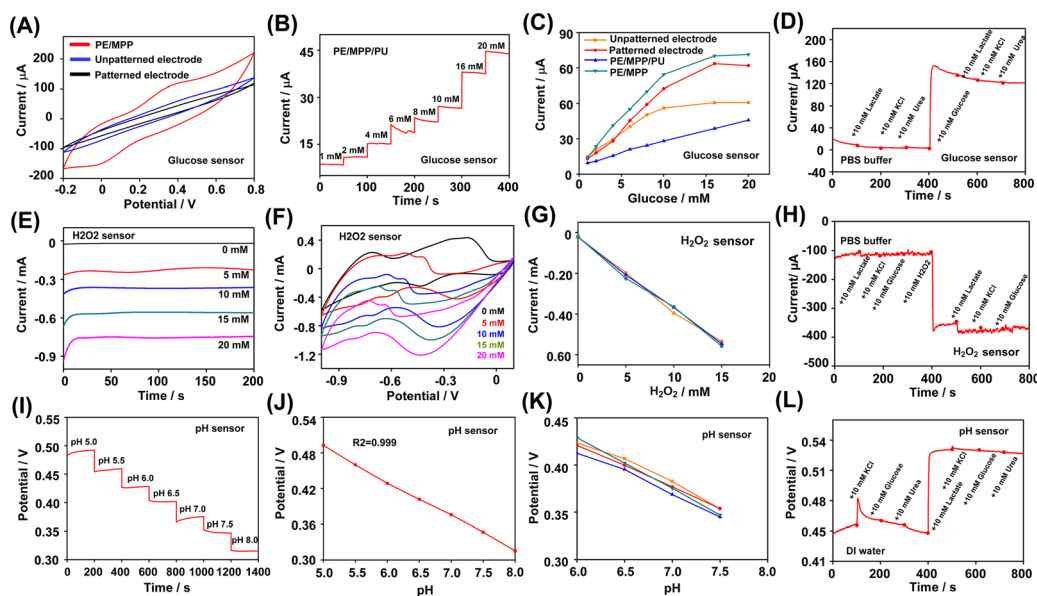
Fig. 4 Electrical performance of patterned electrode sensors. (A) Cyclic voltammetry of different glucose sensors in 10 mM of glucose in $K_3[Fe(CN)_6]$ solutions. PE for the patterned electrode and MPP for MWCNT:PEDOT:PSS. (B) Amperometric responses of the glucose sensor coated with MPP and PU. (C) Linear amperometric responses of glucose sensors with different constructures. (D) The interference study for glucose sensors. Every analyte was added every 50 seconds while keeping the data recording continuous in (D), (H), and (L). (E) Cyclic voltammetry of the H_2O_2 sensor in H_2O_2 solutions from 0 mM to 20 mM. (F) Amperometric responses of the H_2O_2 sensor in H_2O_2 solutions of different concentrations. (G) Reproducibility experiment of H_2O_2 sensors. Reproducibility studies were tested by four reproductions of each type of sensor in (G), and (K). (H) The interference study of H_2O_2 sensors. (I) Chronopotential responses of the pH sensor in solutions. (J) The pH-signal relation of the pH sensor. (K) Reproducibility experiment of pH sensors. (L) The interference study of the pH sensor.

ity (Fig. 4G) and selectivity experiments (Fig. 4H) showed that the biosensor can reliably detect with significant selectivity. The influence of analytes such as glucose on the sensing of H_2O_2 was negligible.

The pH sensor was evaluated in pH buffer solutions. The potential signal changed linearly in the pH range of 5.0–8.0. The calibration curve obtained was in good linearity, with a sensitivity of 58 mV per ΔpH (R_2 = 0.999, RSD = 0.85%, n = 5), which was consistent with the Nernst equation. In order to better characterize the pH sensor, selective experiments were carried out in deionized water. After adding lactic acid, due to the decrease in pH of the solution, the response potential of the electrode significantly increased, while interference substances such as KCl and urea had an impact on the corresponding potential of less than 3%. The counter electrode and reference electrode were also prepared on the same plane substrate as the working electrode. The performance of the integrated glucose sensor, H_2O_2 or pH sensor was further verified (Fig. S4A–C†). The results showed that the integrated three-electrode (for glucose and H_2O_2 detection) and two-electrode (for pH detection) biosensors could detect the corresponding analytes with good sensitivity. The response signal showed good linearity with the change of the analyte concentration.

Validation of the MN-extraction system on the *in vitro* skin model

To obtain continuous concentration information regarding the bio-analytes, stable and reliable biosensors that could provide continuous real-time measurements are necessary. The stability of the MN sensors was tested based on electrochemical detection on an *in vitro* skin model containing 3 mM glucose (Fig. 5A). After the biosensor successfully penetrated the gel sample simulating the skin, negative pressure was applied, and then the extracted liquid contacted the electrode to generate the corresponding electrical signal. As shown in Fig. 5B–D, the stability of the fabricated biosensors was examined by monitoring the chronoamperometric response or chronopotential response of the solution in the phantom gel over 60 min periods at 10 min intervals. In addition, as shown in Fig. 5E–G, the output signals fluctuated only slightly with respect to time, indicating comparatively small variations in the sensor responses in a series of repeated measurements (RSD = 6.46% for glucose sensor; RSD = 8.45% for H_2O_2 sensor; RSD = 2.89% for pH sensor, n = 7). Simultaneous measurements of different analytes were examined when applying three different types of biosensors on the same phantom gel. The selectivity was examined using various concentrations of each analyte. To simulate the variation of bio-analytes, 3 mM glucose, 3 mM lactate, and 300 μM H_2O_2 solutions were alternately injected into the gel and the analyte was allowed to diffuse for several minutes. Then, liquid extraction and electrochemical detection were performed on the MN sensor. As shown in Fig. 5H, the MN-extraction system integrated with the biosensors demonstrated good stability and selectivity in continuous real-time measurement of the corres-

ponding analytes, with limited interference by different analytes.

The skin-penetrating and sensing performance of the MN-extraction system was examined on a cherry tomato and *in vitro* animal tissue, respectively. First, the MN sensor was applied to a cherry tomato while the application of negative pressure assisted the extraction of the ISF, as shown in Fig. S6A.† In the reproducibility experiment, the resulting biosensors showed good stability in monitoring the chronoamperometric responses and chronopotential response of the extracted ISF of the cherry tomato at 5 min intervals (Fig. S6B–D†). The reliability of the MN-extraction system was also validated on *in vitro* animal tissue. A chicken breast was used as the experimental object. The MN sensor was applied to the tissue and negative pressure was used to assist in the extraction of the ISF, as shown in Fig. 5I. In a continuous measurement (Fig. 5J–L), all measurement channels recorded data every five minutes. The MNsensors showed good reproducibility during the test (n = 5) and the recorded signal deviations of the MN-extraction system were less than 10%.

Subsequently, control studies were carried out on the same animal tissue. During the experiment, an amount of solution was injected with a syringe to change the concentration of the tissue fluid. For each test, 400 μL solution of different components was slowly injected into the tissue. The solution was allowed to spread freely for a few minutes before starting the measurement. In the control experiment (Fig. 5M–O) of varying analyte concentrations, when applied to animal tissues *in vitro*, the biosensors showed good dynamic response ability. The corresponding signal change of the biosensors obtained from the control study is shown in Fig. 5P. After the injection of the analyte, the glucose sensor showed a high signal change of up to 150%. Because the concentration of the analytes changed little, the signal changes of the H_2O_2 sensor and pH sensor were relatively small. In general, the extracting and sensing capabilities of the MN extraction system *in vitro* skin models were explored, indicating its potential application in minimally invasive detection.

In vivo testing of the MN-extraction system on rats

After verifying the skin penetration and sensing performance of the MN extraction system *in vitro*, *in vivo* experiments were conducted on rats using the MN extraction system. The rats were anesthetized and hair on the dorsal side was removed, after which the MN sensors were applied. During the measurement, the MN sensor on the back side was properly fixed to avoid interference in the signal recording process. The MN sensor was pressed on the dorsal skin of rats, and the applied MN sensor was withdrawn between measurements. Fig. 6A and B illustrate a MN sensor applied on a rat supported by pressing, and the patterned electrode, which was placed on the back of the MN arrays, acted as a biosensor for electrochemical recording. In addition, the skins on the dorsal side before and after extraction were shown for comparison. It can be seen in Fig. 6C that the applied negative pressure caused
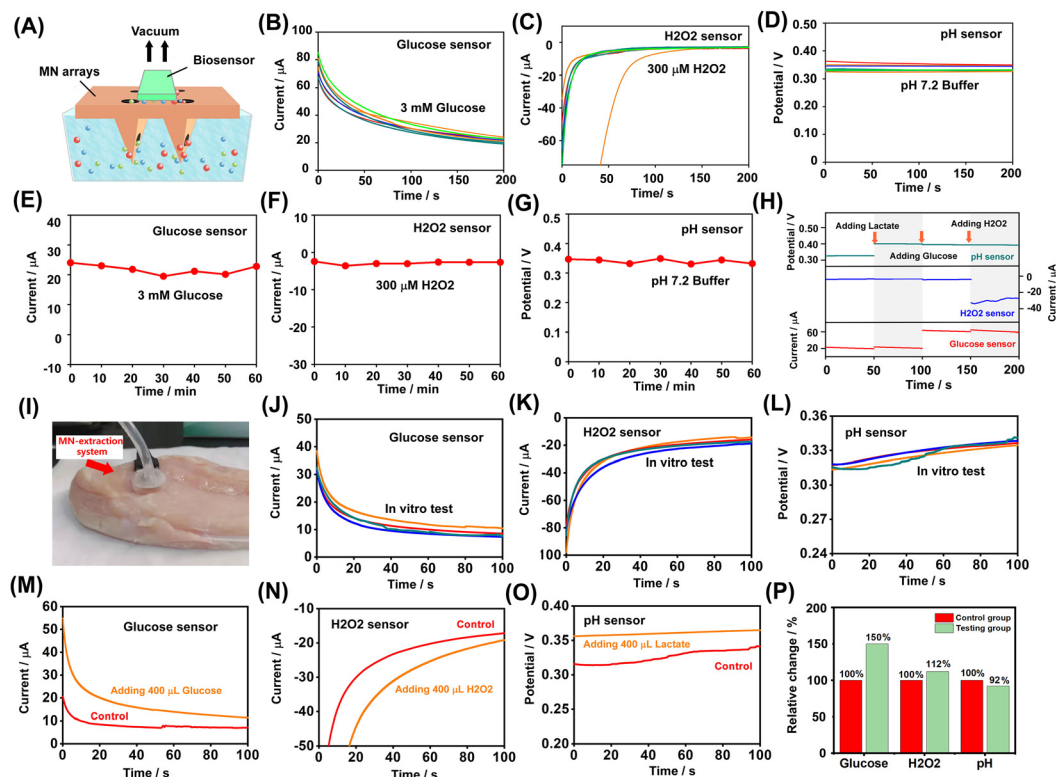
Fig. 5 *In vitro* skin-penetrating and sensing performance test of the microneedle-extraction system. (A) Diagram of skin-mimicking phantom gel by penetrating the MN sensor. A MN sensor was placed on the back of the MN array for sensing. Continuous sensing studies of (B) glucose sensors, (C) H_2O_2 sensors, and (D) pH sensors on *in vitro* skin models. Data were recorded over 60 min periods at 10 min intervals. The corresponding scatter plots of continuous studies of (E) glucose sensors, (F) H_2O_2 sensors, and (G) pH sensors. (H) Interference test results of the microneedle-extraction system. 3 mM glucose, 3 mM lactate, and 300 μM H_2O_2 solutions were alternately injected into the gel. (I) Photograph of an *in vitro* animal tissue applying the MN sensor. (J) Reproducibility studies of the glucose sensor. Reproducibility studies were tested on *in vitro* animal tissue by each type of sensor five times in (J), (K), and (L). Data were recorded at 5 min intervals. Reproducibility studies of the (K) H_2O_2 sensor and (L) pH sensor. (M) Control tests of the glucose sensor. Control tests were tested on animal tissue by injecting different types of analytes in (M), (N), and (O). Control tests of the (N) H_2O_2 sensor and (O) pH sensor. (P) The corresponding signal changes of biosensors were obtained from control tests.
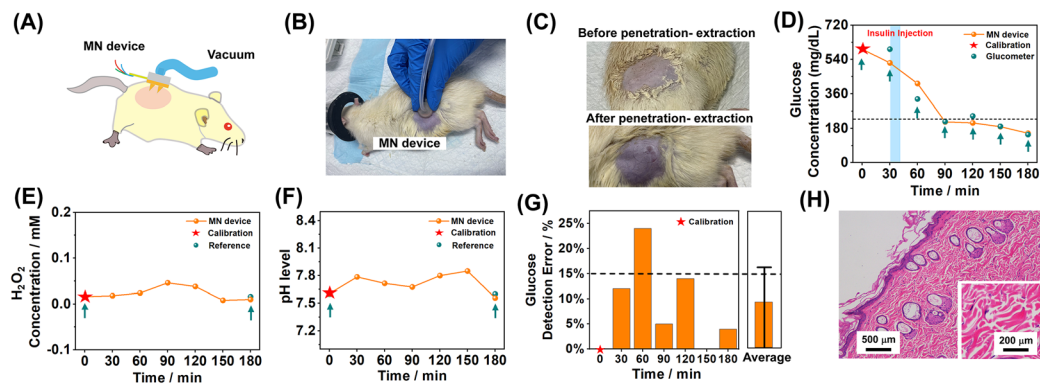
Fig. 6 *In vivo* transdermal detecting of the MN-extraction system integrated with patterned electrodes. (A) Schematic and (B) photography of the MN-extraction system applied on rats. (C) Shaved skin before and after the application of the MN-extraction system for transdermal detection. (D) Glucose concentration was obtained from the applied MN sensor and glucometer. The green arrows indicated the time point of glucometer calibration as a reference. The asterisk indicated the calibration point. The blue block indicated the time interval of insulin injection. The dashed line indicatedthe boundary of normal blood glucose fluctuation (blood glucose level <200 mg dL⁻¹). (E) pH level, and (F) H_2O_2 concentration obtained from the applied MN dsensor and test paper. The green arrows indicated the time point of test paper calibration by reference methods. The asterisk indicated the calibration point. (G) Statistical analysis of detection errors of the glucose sensor of the MN-extraction system compared to those measured using a glucometer at the corresponding time points. The right figure showed the average detection error of the glucose sensor. The asterisks indicated calibration points and the dashed line indicated the clinical criterion of error <15%. (H) Optical microscopic images of skin tissue stained with H&E after treatment with the MN sensor.

mild local skin hyperemia, corresponding to the successful extraction of the ISF by the MN sensor.

After applying negative pressure, the electrical response should be immediately recorded for 3 minutes to ensure the stability of the measured electrochemical signal. The MN-extraction system was used to monitor and measure the fluctuation of glucose, H_2O_2, and pH every 30 minutes. The blood glucose level of the rat was tested with a commercial glucometer in parallel as a reference. The pH values and H_2O_2 levels were recorded by testing isolated serum with a test paper for reference and the isolated serum was extracted from the rat blood by centrifugation. For the MN sensors, the detected amperometric or potentiometric signals were converted to the corresponding glucose, H_2O_2, or pH concentrations and were further calibrated by the extra blood reference data on the first time-point, to eliminate the difference between *in vitro* and *in vivo* test environments. At the time point of 30 min, 80 μL of 4 mg mL^{-1} insulin was administered *via* intramuscular injection, allowing 30 min for insulin to take effect and lead to the decrease of blood glucose. As shown in Fig. 6D, the glucose level measured by the MN sensor showed a good correlation with those measured using the commercial glucometer. The pH values (Fig. 6E) and H_2O_2 level (Fig. 6F) were also *in situ* monitored using the MN-extraction system during the experiment. After the injection of insulin, the glucose level of the rat with diabetes showed a significant decrease and was reduced to the normal glucose level within one hour, while the H_2O_2 and pH levels showed only slight changes during the measurement. The detected average glucose level was reduced by ~405 mg dL^{-1} after insulin injection, and this result was consistent with the results (glucose level reduced by ~430 mg dL^{-1}) detected using a commercial glucometer. The detection error of all the MN-extraction-system-measured glucose signals was below 25%, with an average error of 7.83% ± 9.7%. It was corresponding to a sensing error <20% that was closely satisfying the clinical standard of error <15%.

After 12 h, the skin tissue, where the MN sensor was applied, was sectioned and then stained with H&E. The MN-treated skin tissue did not show obvious infiltrated inflammatory cells in the field of the microscope, as shown in Fig. 6G, indicating that no significant skin irritation was induced from the application of the MN-extraction system. Overall, the *in vivo* test results suggested that the bio-analyte levels in the ISF detected using the MN sensor were consistent with those found in blood, which suggested a successful *in vivo* application of the MN-extraction system.

Conclusion

In this work, we demonstrated the development of an MN extraction system integrated with patterned electrodes for minimally invasive transdermal detection. This system consisted of patterned electrodes, MN arrays, and three bio-analytes (including glucose, pH, and H_2O_2) which were targeted as representative factors for assessing sensor performance. 3D-printed MN arrays for penetrating the skin were assembled with patterned electrodes, while an external air extraction device was integrated to provide negative pressure for the extraction of the ISF. Patterned electrodes with micropillar structures were prepared to increase the surface area for enzyme coating. In order to further improve the electrichemical performance of the sensor, a MWCNT:PEDOT:PSS layer was deposited on the electrode surface. The *in vitro* experimental characterization of the sensors revealed good sensitivity, selectivity, and stability. The *in vivo* application of the MN sensor in rats showed that it can detect the fluctuations of different bio-analytes *in situ*, and the results were consistent with those in blood. This MN-extraction system showed its potential for *in vivo* on-demand detection, with minimal damage to tissues. Further efforts should be devoted to improving system functionalities and applying them to a wider range of analyte detection for the sake of better healthcare monitoring.

Method

Materials

Polyaniline emeraldine (PANI), poly (vinyl butyral) resin BUTVAR B-98 (PVB), methanol, multi-walled carbon nanotubes (MWCNTs), poly (sodium 4-styrenesulfonate) (NaPSS), 3,4-ethylenedioxythiophene (EDOT), glutaraldehyde, bovine serum albumin (BSA), dimethyl sulfoxide (DMSO), tetrahydrofuran, dimethylformamide, polyurethane (PU), glucose, 3% H_2O_2, urea, lactate, sodium chloride (NaCl), and potassium chloride (KCl) were obtained from Sigma Aldrich. Polydimethylsiloxane (PDMS) with its curing agent, SU-8 2015 photoresist SU-8 developer, and UV-curable resin liquid (Formslab, USA) were purchased from Dow Corning (USA). Glucose oxidase (GOx, >100 activity units per milligram) and rhodamine B were purchased from Aladdin Reagents. Ag/AgCl conductive inks were purchased from Australian Laboratory Services (ALS). Standard glass slides (100 mm × 100 mm, 1 mm thick) were purchased from CITOTEST (China), and phosphate-buffered saline (PBS) (pH 7.2) was purchased from Life Science. Solutions were prepared using deionized water (18.3 MΩ cm) obtained using the Millipore water purification system.

Fabrication of the patterned substrate

The micro-nanostructure was prepared on the surface of the electrodes by photolithography. A standard glass slide (100 mm × 100 mm, 1 mm thick) was used as the substrate for fabrication. First, the cleaned glass slide was spin-coated with a 20-μm-thick SU-8 2015 photoresist layer at 2000 rpm. After the material was soft-baked at 95 °C for 3.5 min and exposed to a UV dose of 145 mJ cm^{-2} using an i-line mask aligner (ABM, USA), it was subjected to post-exposure baking for 4.5 min. The glass slide was then developed for 3.5 min using an SU-8 developer, followed by post-development baking at 200 °C for 30 min. The SU-8 mold was used for casting flexible PDMS film. The combination of PDMS with its curing agent

(10 : 1) formed an even mixture, which was poured into the SU-8 mold and dried at 80 °C for over 3 h. Subsequently, the UV-curable resin liquid was cast into the PDMS film mold and exposed to UV light to prepare the designed pattern. Lastly, the resin substrate was sputtered with Pt (20 min, thickness >100 nm) to fabricate lead and pad patterns.

Preparation of Ag/AgCl and Pt coating on the resin substrate

Through the use of a designed metal pattern, Ag/AgCl and Pt were coated onto the substrate, such that the coatings were constrained to certain areas. The Ag/AgCl reference electrode was prepared *via* dip-coating to produce an Ag/AgCl layer coated onto the patterned resin substrate. A reserved patch was immersed in the Ag/AgCl conductive ink to deposit Ag/AgCl film onto the resin substrate. 5 μL PVB solution (79.1 mg PVB and 50 mg of NaCl into 1 ml methanol) was cast on the Ag/AgCl reference electrode to minimize the potential shift.[38] Simultaneously, the Pt counter electrode was prepared with the fabrication of the lead and pad patterns from the resin substrate.

Preparation of the glucose sensor

The patterned substrate coated with Pt was subjected to electrodeposition with MWCNT:poly(3,4-ethylenedioxythiophene) (PEDOT):polystyrene sulfonate (PSS) (MWCNT:PEDOT:PSS, or MPP) *via* cyclic voltammetry sweeping (0–0.95 V) for 20 cycles in a mixture of PSS (0.1 M), EDOT (20 mM), and MWCNT (2 mg mL^{-1}), in accordance with an existing modified process.[39] After the electrode was washed and dried in air, a 10 μl of solution comprising GOx (100 mg mL^{-1} in PBS), glutaraldehyde (2.5% in PBS), and BSA (80 mg mL^{-1} in PBS) was drop-cast onto the resin electrode and then allowed to dry overnight. The electrode was then rinsed with PBS to remove uncrosslinked enzymes remaining on the surface. To achieve a linear response in higher concentrations, a 10 μL of PU solution (0.6 g PU dissolved in 10 g tetrahydrofuran/dimethylformamide solution with a mass ratio of 98 : 2) was drop-cast on the surface of the electrode. Notably, the glucose sensor, as an enzyme-based sensor, must be stored at 4 °C to maintain the enzyme activity.

Preparation of the H$_2$O$_2$ sensor

The patterned resin substrate was used as the H$_2$O$_2$ sensor, where the Pt electrode served as the working electrode.

Preparation of the pH sensor

The fabrication procedure for the pH sensor was slightly modified in accordance with a protocol detailed in a previous study.[40] First, 25 mg of the PANI base was dissolved in 25 ml of DMSO to prepare 1 mg ml^{-1} PANI solution, which was stirred evenly before use. Then, 10 μL of PANI solution (ion-selective membrane) was drop-cast onto the resin electrode and exposed and baked at 40 °C for at least 3 h. The resin electrode was then placed into a vacuum chamber with HCl. In the vacuum, the HCl vapor introduced H$^+$ into the PANI base film. After the doping process, the patterned electrode was washed

with deionized water at least three times and then blow-dried with N$_2$.

Mechanical characterization of 3D-printed MN arrays

The MN arrays, fabricated by 3D printing, were purchased from Botai 3D Technology (China). To validate the mechanical properties, a piece of cleaned pigskin was placed onto a glass slide and the MN arrays were attached to a control lever of a mechanical test bench (Daheng). The control lever was used to lower the MN until the pigskin was pierced. The drop speed of the control lever was set to 0.29 mm s^{-1}. After successful penetration, the microneedle remained in its original position for several seconds, and then rose at the same speed as the control lever. The overall stress condition of the MN arrays was recorded using the running mechanical test bench.

Characterization of MN arrays for their penetration into tissue

The MN arrays were treated with air plasma (80 W, 3 min) to enhance their hydrophilicity, after which the tips of the MN arrays were soaked in 1 mg mL^{-1} of rhodamine B to enable fluorescence labeling. Subsequently, the pre-dyed MN arrays were pressed against a piece of cleaned pigskin for 3 min and withdrawn. The processed tissue was observed *via* inverted fluorescence microscopy (MSHOT MF41). After the penetration of MN arrays, the pigskin was cut into 2 mm slices to enable the imaging of the area penetrated by the MN with inverted fluorescence microscopy.

Water extraction capacity of MN arrays

Before the characterization of water extraction capacity, the MN arrays were assembled with PDMS to improve air tightness. A dry sponge was placed on the top of MN arrays, which were then placed in a chamber filled with water. When a certain negative pressure (7.5 or 15 cmHg) was applied, an amount of water was extracted from the chamber and absorbed by the sponge. The amount of extracted water can be obtained as the difference between the masses of the sponge before and after water absorption.

Electrochemical characterization of biosensors with the patterned electrodes *in vitro*

Electrochemical characterization experiments were conducted *via* a standard three-electrode system using an electrochemical analyzer, CHI 760E (CH Instruments, China). For the glucose and H$_2$O$_2$ sensors, electrical characterization was performed *in vitro* using 10 mM of PBS (pH 7.2). The cyclic voltammetry scanning of the glucose sensor was performed in a glucose/ K$_3$[Fe(CN)$_6$] solution (5 mM K$_3$[Fe(CN)$_6$], 5 mM K$_4$[Fe(CN)$_6$], and 0.1 M of KCl in deionized water). For the pH sensor, various solutions in the pH range of 5–8 were used to formulate freshly prepared buffer solutions. Before use, the pH of each solution was measured using a commercial pH meter as a reference. The reliability, selectivity, and stability of the patterned electrode sensors were verified. The effects of electroactive interferents, such as urea, KCl, and lactate, on the biosensor, were analyzed. The corresponding chronoampero-

metric signal of the glucose channel was recorded at 0.6 V, whereas the corresponding signal of the H_2O_2 channel was recorded at −0.45 V. The potential signal of the pH channel was measured in Open Circuit Potential-Time mode. The process of obtaining electrical signals possessed a signal stabilization period of 200 s.

Skin-penetrating and sensing performance tests

To simulate human skin, soft agarose phantom gel was prepared to simulate tissue[11,41,42] and evaluate the performance of the MN-extraction system. To prepare the agarose phantom gel, 140 mg of agarose powder was added to 10 mL of PBS (1.4%). The agarose solution was stirred at 95 °C until the agarose was completely dissolved. Subsequently, the uniformly dissolved agarose solution was poured into a mold and cooled to solidify at room temperature. The agarose phantom gel was then rinsed with PBS for skin model evaluation. Before the MN sensor was used, 3 mM glucose solution was diffused in the agarose phantom gel. Each MN sensor was placed on the agarose phantom gel, and negative pressure was applied to extract the liquid. For long-term continuous studies, each MN sensor was allowed to measure the corresponding bio-analytes over 100 min periods at 10 min intervals. Subsequently, 1 mL volumes of 3 mM glucose, 3 mM lactate, and 300 μM H_2O_2 solutions were alternately added to the agarose phantom gel at 10 min intervals (after each addition, the additives were allowed to diffuse for 15 min). The analytes were then allowed to spread over several minutes to generate responding electrical signals on the sensor.

Next, a cherry tomato and a piece of *in vitro* animal tissue (chicken breast) were used as tissue models to further evaluate the skin-penetrating and sensing performance of the MN-extraction system, respectively. The cherry tomato and chicken breast were purchased from a market. To measure skin-penetrating performance, each MN sensor was used on the cherry tomato, and negative pressure was applied to extract the ISF. Then, each MN sensor was allowed to measure the corresponding bio-analytes at 5 min intervals. To measure the sensing performance, a chicken breast was treated with a MN sensor for skin model evaluation. Similarly, each MN sensor was allowed to measure the corresponding bio-analyte at 5 min intervals. Afterward, 400 μL of 1M glucose, 1M lactate, and 500 mM H_2O_2 solutions were separately added to the chicken breast and allowed to diffuse for 15 min.

In vivo testing of the MN-extraction system

Sprague Dawley (SD) rats (SPF grade) weighing 250 g with diabetes (Animal Center, Sun Yat-Sen University, Guangzhou, China) were used for experiments. Before the measurement, the rats were anesthetized with 2% isoflurane, and the hair on their dorsal side was removed using a hair removal cream. The MN sensor was then applied to the dorsal side of the skin. By alternately applying three MN sensors, electrochemical signals were recorded. *In vivo* electrochemical measurements were performed by recording the amperometric or potential signals. The glucose concentrations were obtained from both the MN

sensor and were compared with results obtained from a glucometer as reference. Moreover, the H_2O_2 and pH values of blood were obtained by testing isolated serum with a test paper for reference. For the MN sensor, the recorded signals were converted to the corresponding glucose, H_2O_2, or pH levels by the vitro standard curves. The concentrations measured by the MN system were further calibrated by the blood reference data on the first time-point so that the difference between *in vitro* and *in vivo* experiments could be eliminated. All animal procedures in this study were performed in accordance with the Guidelines for Care and Use of Laboratory Animals of Sun Yat-Sen University and approved by the Institutional Animal Care and Use Committee, Sun Yat-Sen University (Approval No. SYSU-IACUC-2021-000612).

Biocompatibility tests of MN applications

Local skin irritation induced by the application of the MN sensor was tested. MN sensors were applied to the backs of rats for 3 h. Then, the MN sensor were removed, and the rats were allowed to return to the cage. After 12 h, the MN-treated local skin tissue was sectioned and then stained with hematoxylin and eosin (H&E). The tissue profile was examined with optical microscopy (MSHOT).

Author contributions

Conceptualization: Changyuan Zhan, Xi Xie, and Hui-Jiuan Chen; methodology: Xi Xie and Hui-Jiuan Chen; investigation: Changyuan Zhan, Zhiran Shen, Xinshuo Huang, Shuang Huang, Xiangling Li, Xi Xie, and Hui-Jiuan Chen; experimental development and data analysis: Changyuan Zhan, Shuang Huang, and Xiangling Li; writing—original draft preparation: Changyuan Zhan and Hui-Jiuan Chen; writing—review and editing: Changyuan Zhan, Xi Xie, and Hui-Jiuan Chen; supervision: Xi Xie and Hui-Jiuan Chen; project administration: Xi Xie and Hui-Jiuan Chen; funding acquisition: Fanmao Liu, Jing Liu, Jiang Yang, Jiefeng Xu, Xi Xie, and Hui-Jiuan Chen. All authors have read and agreed to the published version of the manuscript.

Conflicts of interest

The authors declared that they had no known competing financial interests or personal relationships that could have appeared to influence the work reported in this paper.

Acknowledgements

References

1 W. Jung, *et al.*, Point-of-care testing (POCT) diagnostic systems using microfluidic lab-on-a-chip technologies, *Microelectron. Eng.*, 2015, **132**, 46–57.

2 D. Wang, *et al.*, Recent developments in microfluidic–based point–of–care testing (Poct) diagnoses, *Nanotechnol. Microfluid.*, 2020, 239–280.

3 A. Trautmann, *et al.*, Towards a versatile point-of-care system combining femtosecond laser generated microfluidic channels and direct laser written microneedle arrays, *Microsyst. Nanoeng.*, 2019, **5**(1), 1–9.

4 P. B. Luppa, *et al.*, Point-of-care testing (POCT): Current techniques and future perspectives, *TrAC, Trends Anal. Chem.*, 2011, **30**(6), 887–898.

5 E. Matteucci and O. Giampietro, Point-of-care testing in diabetes care, *Mini-Rev. Med. Chem.*, 2011, **11**(2), 178–184.

6 M. Gong, *et al.*, Flexible breathable nanomesh electronic devices for on–demand therapy, *Adv. Funct. Mater.*, 2019, **29**(26), 1902127.

7 Y. Yamamoto, *et al.*, Printed multifunctional flexible device with an integrated motion sensor for health care monitoring, *Sci. Adv.*, 2016, **2**(11), e1601473.

8 B. Paul, *et al.*, Printed Iontophoretic–Integrated Wearable Microfluidic Sweat–Sensing Patch for On–Demand Point–Of–Care Sweat Analysis, *Adv. Mater. Technol.*, 2021, **6**(4), 2000910.

9 M. R. Prausnitz, Microneedles for transdermal drug delivery, *Adv. Drug Delivery Rev.*, 2004, **56**(5), 581–587.

10 Y.-C. Kim, J.-H. Park and M. R. Prausnitz, Microneedles for drug and vaccine delivery, *Adv. Drug Delivery Rev.*, 2012, **64**(14), 1547–1568.

11 Y. Gao, *et al.*, PEGDA/PVP microneedles with tailorable matrix constitutions for controllable transdermal drug delivery, *Macromol. Mater. Eng.*, 2018, **303**(12), 1800233.

12 T. Waghule, *et al.*, Microneedles: A smart approach and increasing potential for transdermal drug delivery system, *Biomed. Pharmacother.*, 2019, **109**, 1249–1258.

13 Z. Zeng, *et al.*, Fabrication of gelatin methacryloyl hydrogel microneedles for transdermal delivery of metformin in diabetic rats, *Bio-Des. Manuf.*, 2021, **4**(4), 902–911.

14 P. Bollella, *et al.*, Microneedle-based biosensor for minimally-invasive lactate detection, *Biosens. Bioelectron.*, 2019, **123**, 152–159.

15 Y. Li, *et al.*, Fabrication of sharp silicon hollow microneedles by deep-reactive ion etching towards minimally invasive diagnostics, *Microsyst. Nanoeng.*, 2019, **5**(1), 1–11.

16 Y. Liu, *et al.*, Continuous monitoring of diabetes with an integrated microneedle biosensing device through 3D printing, *Microsyst. Nanoeng.*, 2021, **7**(1), 1–12.

17 M. T. McCrudden, *et al.*, Microneedle applications in improving skin appearance, *Exp. Dermatol.*, 2015, **24**(8), 561–566.

18 S. Bhatnagar, K. Dave and V. V. K. Venuganti, Microneedles in the clinic, *J. Controlled Release*, 2017, **260**, 164–182.

19 H. Lee, *et al.*, A graphene-based electrochemical device with thermoresponsive microneedles for diabetes monitoring and therapy, *Nat. Nanotechnol.*, 2016, **11**(6), 566–572.

20 H. Lee, *et al.*, Wearable/disposable sweat-based glucose monitoring device with multistage transdermal drug delivery module, *Sci. Adv.*, 2017, **3**(3), e1601314.

21 K. Takeuchi, *et al.*, Microfluidic chip to interface porous microneedles for ISF collection, *Biomed. Microdevices*, 2019, **21**(1), 1–10.

22 M. Zheng, *et al.*, Osmosis–powered hydrogel microneedles for microliters of skin interstitial fluid extraction within minutes, *Adv. Healthcare Mater.*, 2020, **9**(10), 1901683.

23 R. He, *et al.*, A Hydrogel Microneedle Patch for Point–of–Care Testing Based on Skin Interstitial Fluid, *Adv. Healthcare Mater.*, 2020, **9**(4), 1901201.

24 X. Huang, *et al.*, Minimally invasive technology for continuous glucose monitoring, *Bio-Des. Manuf.*, 2022, **5**(1), 9–13.

25 C. G. Li, *et al.*, An optimized hollow microneedle for minimally invasive blood extraction, *Biomed. Microdevices*, 2013, **15**(1), 17–25.

26 P. Xue, *et al.*, Blood sampling using microneedles as a minimally invasive platform for biomedical diagnostics, *Appl. Mater. Today*, 2018, **13**, 144–157.

27 S. N. Economidou and D. Douroumis, 3D printing as a transformative tool for microneedle systems: Recent advances, manufacturing considerations and market potential, *Adv. Drug Delivery Rev.*, 2021, **173**, 60–69.

28 C. G. Li, *et al.*, One-touch-activated blood multidiagnostic system using a minimally invasive hollow microneedle integrated with a paper-based sensor, *Lab Chip*, 2015, **15**(16), 3286–3292.

29 K. W. Ng, W. M. Lau and A. C. Williams, Towards pain-free diagnosis of skin diseases through multiplexed microneedles: biomarker extraction and detection using a highly sensitive blotting method, *Drug Delivery Transl. Res.*, 2015, **5**, 387–396.

30 X. Zhang, *et al.*, Encoded microneedle arrays for detection of skin interstitial fluid biomarkers, *Adv. Mater.*, 2019, **31**(37), 1902825.

31 C. Kolluru, *et al.*, Monitoring drug pharmacokinetics and immunologic biomarkers in dermal interstitial fluid using a microneedle patch, *Biomed. Microdevices*, 2019, **21**, 1–9.

32 G.-S. Liu, *et al.*, Microneedles for transdermal diagnostics: Recent advances and new horizons, *Biomaterials*, 2020, **232**, 119740.

33 D. A. Muller, *et al.*, Surface modified microprojection arrays for the selective extraction of the dengue virus NS1

protein as a marker for disease, *Anal. Chem.*, 2012, **84**(7), 3262–3268.

34 A. V. Mohan, *et al.*, Continuous minimally-invasive alcohol monitoring using microneedle sensor arrays, *Biosens. Bioelectron.*, 2017, **91**, 574–579.

35 F. Tehrani, *et al.*, An integrated wearable microneedle array for the continuous monitoring of multiple biomarkers in interstitial fluid, *Nat. Biomed. Eng.*, 2022, 1–11.

36 Y. Shao, *et al.*, Bioinspired 3D-Printed MXene and Spidroin-Based Near-Infrared Light-Responsive Microneedle Scaffolds for Efficient Wound Management, *ACS Appl. Mater. Interfaces*, 2022, **14**(51), 56525–56534.

37 A. Keirouz, *et al.*, Conductive Polymer–Coated 3D Printed Microneedles: Biocompatible Platforms for Minimally Invasive Biosensing Interfaces, *Small*, 2023, 2206301.

38 W. Gao, *et al.*, Fully integrated wearable sensor arrays for multiplexed in situ perspiration analysis, *Nature*, 2016, **529**(7587), 509–514.

39 Z. Lu, *et al.*, PtNPt/MWCNT-PEDOT: PSS-Modified Microelectrode Arrays for the Synchronous Dopamine and Neural Spike Detection in Rat Models of Sleep Deprivation, *ACS Appl. Bio Mater.*, 2021, **4**(6), 4872–4884.

40 R. Rahimi, *et al.*, A low-cost flexible pH sensor array for wound assessment, *Sens. Actuators, B*, 2016, **229**, 609–617.

41 K. Y. Goud, *et al.*, Wearable electrochemical microneedle sensor for continuous monitoring of levodopa: toward Parkinson management, *ACS Sens.*, 2019, **4**(8), 2196–2204.

42 H. Chang, *et al.*, A swellable microneedle patch to rapidly extract skin interstitial fluid for timely metabolic analysis, *Adv. Mater.*, 2017, **29**(37), 1702243.